9 Tandem Configuration in Cruise Conditions

In this chapter, a simplified tandem cruising configuration is examined in the wind tunnel using PIV. Shed LEVs and TEVs are tracked over moving fore- and hindfoils emulating dragonfly flight at high speeds. A standard control-volume analysis is used to extract mean forces for the two configurations and various airfoil phasings tested. These cases have also been simulated using a simple URANS methodology, as described in section 4.3. Insight obtained from these simulations is used to access potential advantages in comparison to the single-airfoil case.

9.1 Parameter Space

For all tandem cases the forefoil (F) was operated with a constant sinusoidal pure-plunge motion at $k = 0.25$:

$$h_F = h_o \cos(2\pi f t). \tag{9.1}$$

The pitching and plunging movement of the hindfoil (H) followed Eq. (9.2)-(9.3), where the hindfoil lead the forefoil motion with a phase angle ψ:

$$h_H = h_o \cos(2\pi f t + \psi) \tag{9.2}$$

$$\alpha_H = \alpha_o + \alpha_1 \cos(2\pi f t + \phi + \psi) \tag{9.3}$$

Two sets of measurements were performed, one with a pure-plunging hindfoil (presented in section 9.2) and the other with a pitching/plunging hindfoil (see section 9.3). For the latter, pitching lead plunging by a phase angle of $\phi = 90°$ ensuring optimal thrust efficiency. The pitch/plunge motion is characterized by lower effective angles of attack throughout the cycle and therefore less separation when compared to the pure-plunging motion. The mean angle of attack for both fore- and hindfoils was fixed at $\alpha_o = 8°$, whereby the pitching amplitude in section 9.3 was set to $\alpha_1 = 8.42°$. Both individual pure-plunge and pitch/plunge kinematics have been examined in detail by Ol et al (2009) and therefore serve as useful reference cases.

The dimensionless plunge amplitude for all cases, based on the quarter-chord position ($c/4$), was maintained at $h = \pm 0.5\,c$. The rotation points for both fore- and hindfoil were fixed at the quarter-chord position as well. Airfoil spacing was set to $S = 2\,c$ between the airfoil quarter-chord positions. The airfoil phasing (ψ) was varied in 30° increments starting with an in-phase movement of $\psi = 0°$ up to $\psi = 120°$, representative of the phasing used in dragonfly flight, see Azuma and Watanabe (1988).

9.2 Hindfoil with Pure-Plunge

9.2.1 Vortex Trajectories and Convective Velocities

In Fig. 9.1(a) one can observe that the plunging hindfoil has a large influence on the LEV trajectories. The similar upward deflection was measured for the static-hindfoil cases, as reported on in section 8.2.1. For the plunging hindfoil, however, the LEV convects over the hindfoil during the upstroke, thus leading to an even higher deflection in the

vortex trajectory. After passing the hindfoil trailing edge, the LEVs are then shifted downwards again due to the overall downwash of the lift-producing hindfoil. Note that for a high phase lag between the airfoils the LEV passes very close to the leading edge of the hindfoil ($\psi = 90°$) or even hits the hindfoil leading edge ($\psi = 120°$), thus leading to a quick disintegration of the vortex. This vortex-impingement phenomenon is described in Rockwell (1998).

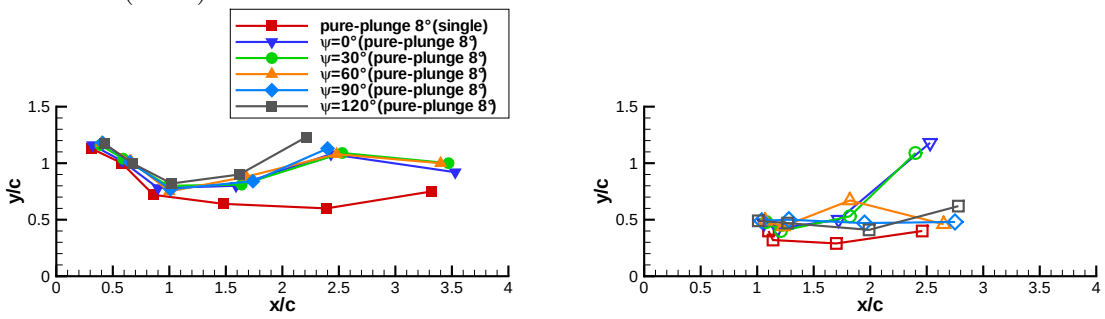

(a) LEV position

(b) TEV position

Figure 9.1: Trajectories of LEV and TEV cores for hindfoil with pure-plunge motion.

For $\psi = 0°$ and $\psi = 30°$ the TEV passes together with the LEV above the hindfoil (see $\psi = 30°$ in Fig. 9.2). One can observe a strong upward deflection of the TEV for these cases. This is explained by the superposition of two effects; first the upward induction of the LEV, and second, the strong circulation of the hindfoil.

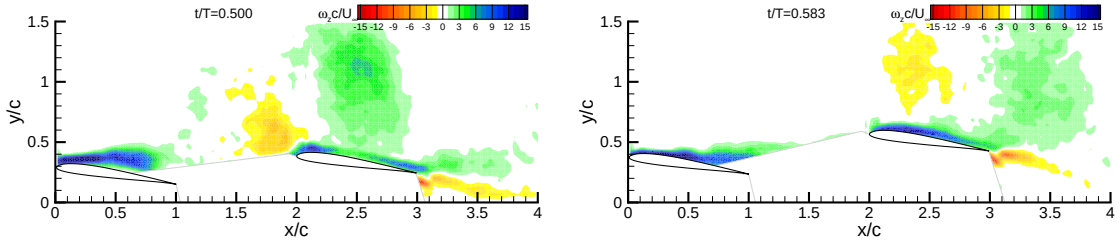

Figure 9.2: Plunging hindfoil with $\psi = 30°$; LEV and TEV passing above the hindfoil.

When examining the vortex velocities in Fig. 9.3, one can observe that the overall LEV convection deviates only for cases $\psi = 90°$ and $\psi = 120°$. In contrast, for the TEV convection only the $\psi = 30°$ case varies from the reference values. These variations in convective velocities are due to strong viscous interactions with the hindfoil, which have been discussed in detail in section 8.2.1.

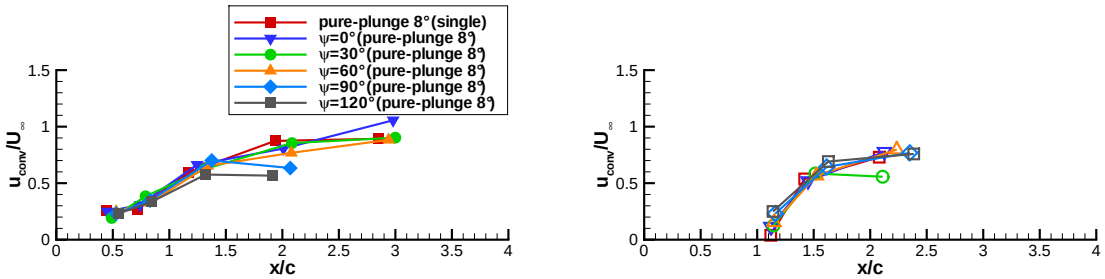

(a) LEV convection velocity

(b) TEV convection velocity

Figure 9.3: Convective velocity of LEV and TEV cores for the cases with the hindfoil performing pure-plunge.

9.2.2 Vortex-Induced Separation

Vortex-induced separation, as described in section 8.2.1, occurs in the pure-plunge tandem airfoil configuration but only for a phase lag of $\psi = 0°$. For the higher phase lags ($\psi \geq 30°$) the phenomenon was not observed. The overall strength of the induced vortex is lower than with the static hindfoil case with $h/c = -0.5$ and $\alpha_H = 8°$ and is shown for comparison in Fig. 9.4.

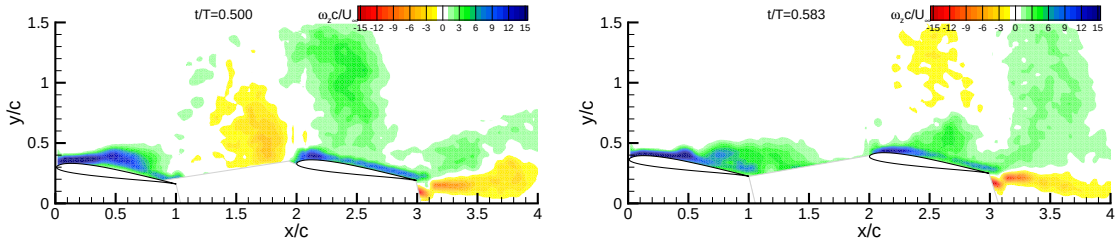

Figure 9.4: Forefoil and hindfoil performing pure-plunge motion with $\psi = 0°$; development and convection of induced vortex over the hindfoil surface clearly seen as TEV passes by.

9.2.3 LEV Circulation

As observed in section 8.2.2 for the Schmidt propeller configuration, the tandem arrangement has the effect of strengthening the LEV over the forefoil, see Fig. 9.5(a). In Fig. 9.5(b), the equivalent formation time is plotted; see section 2.3.1 for a detailed explanation of this concept. An increase in the formation number to $\hat{T} > 6$ for the tandem cases clearly identifies the manipulation of the limiting vortex-formation process through temporal and spatial variation of the feeding shear layer, as discussed in Dabiri (2009).

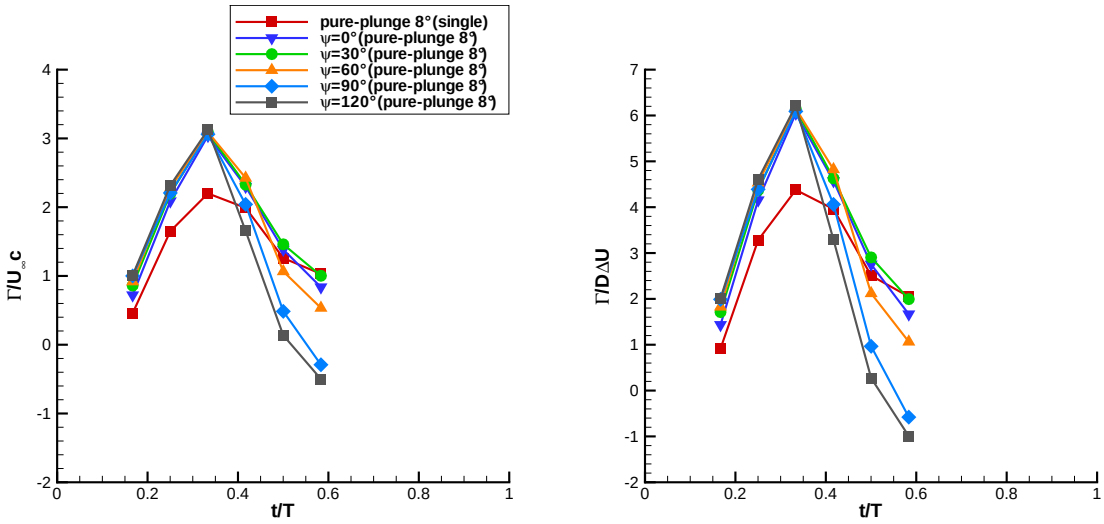

(a) circulation

(b) formation time

Figure 9.5: Development of LEV circulation (left) and formation time (right) as a function of period for the various tandem-airfoil configurations.

9.2.4 Control-Volume Analysis

When applying a quasi-steady control-volume analysis, as described in section 3.7.3, one obtains a representative variation of lift and drag with time, see Fig. 9.6. The curves are

insightful albeit shifted later in phase due to the delay in the convection of information to the back surface of the control volume. Lift generation appears to be more constant for higher phasings whereas for drag lower phasings appear more advantageous.

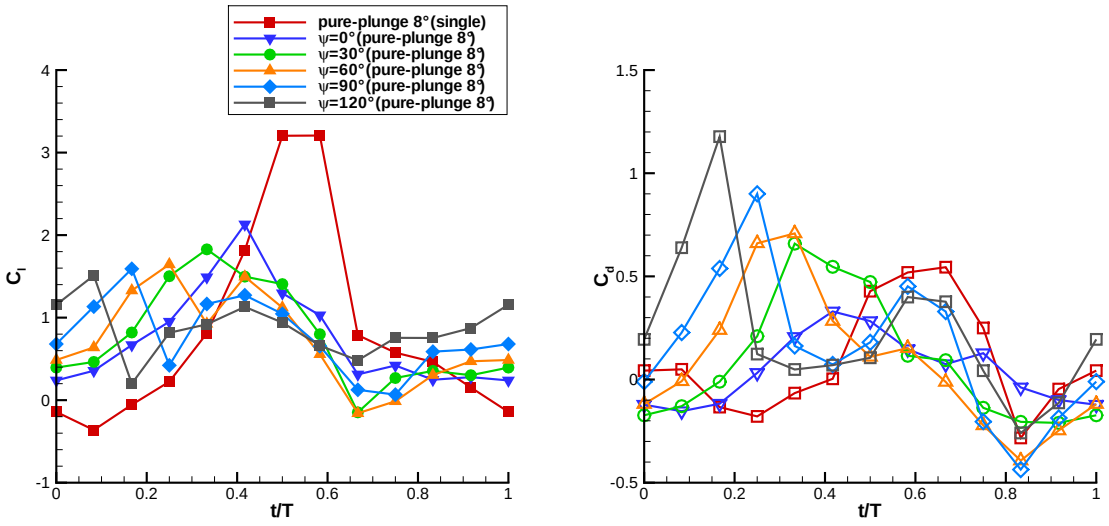

(a) lift variation

(b) drag variation

Figure 9.6: Lift and drag variation over cycle using the standard control-volume analysis; note t/T referenced to the forefoil position.

9.2.5 Pressure Integration

Using the pressure-integration methodology outlined in section 8.2.5, the pressure distributions over the hindfoil suction side at the bottom-dead-center position ($t/T = 0.5$) and one time step thereafter ($t/T = 0.567$) have been calculated, see Fig. 9.7. At these positions, an induced suction due to the passing wake helps reduced the aerodynamic power needed by the system, as described in Lehmann (2009). The tandem-airfoil cases show a distinctly higher suction, particularly when compared to the single-airfoil (reference) case.

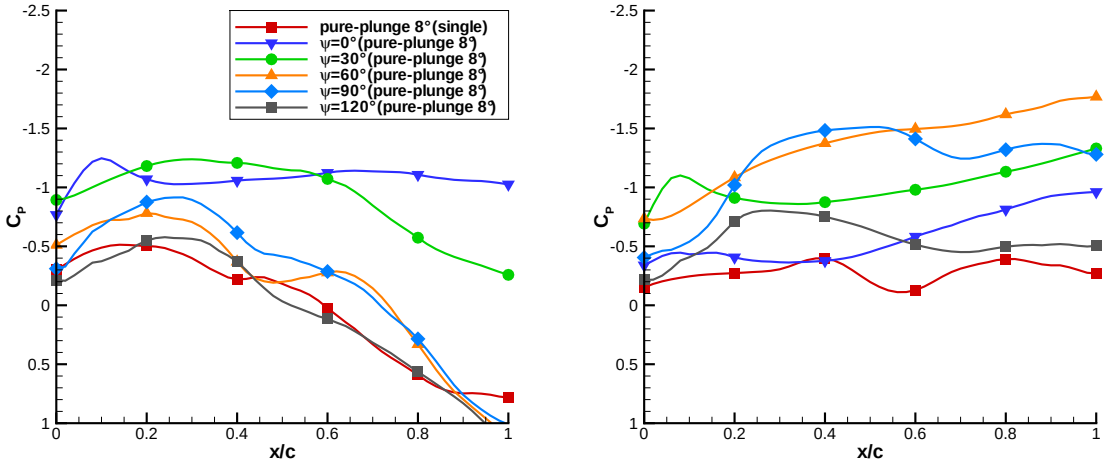

(a) $t/T = 0.500$

(b) $t/T = 0.567$

Figure 9.7: Pressure distributions over hindfoil suction surface at stroke reversal.

9.3 Hindfoil with Pitch/Plunge

9.3.1 Vortex Trajectories and Convective Velocities

The LEV and TEV trajectories for the tandem cases with a pitching and plunging hindfoil, as presented in Fig. 9.8, are qualitatively very similar to the tandem cases with a pure-plunging motion (compare with Fig. 9.1). Again one can see that for $\psi = 90°$ and $\psi = 120°$ the LEV breaks up upon contact with the hindfoil leading edge, as shown in Fig. **??**. For higher phase angles of $\psi = 60°$, $\psi = 90°$ and $\psi = 120°$ the TEV passes below the hindfoil, as shown exemplarily for $\psi = 120°$ in Fig. 9.9.

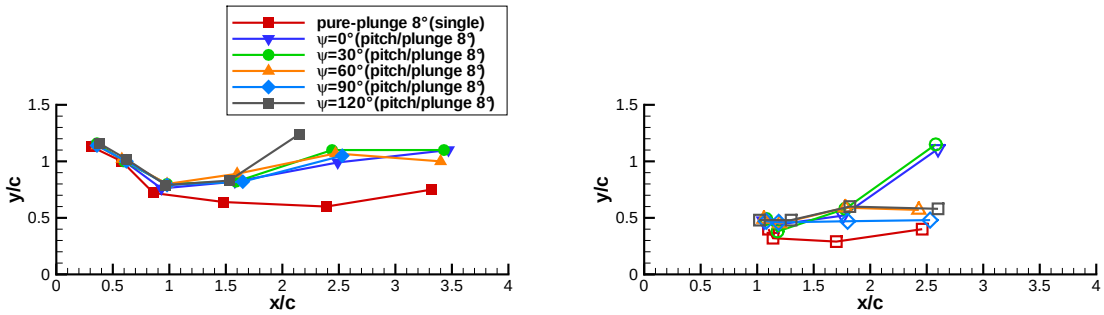

(a) LEV position

(b) TEV position

Figure 9.8: Trajectories of LEV and TEV cores for the pitch-plunge cases.

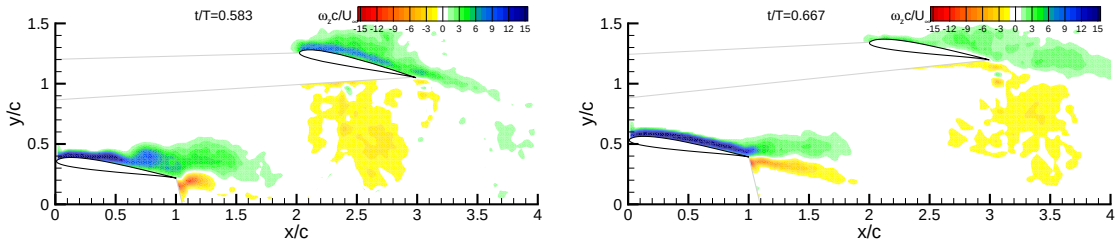

Figure 9.9: Hindfoil performing pitch/plunge with $\psi = 120°$; plots showing the TEV passing below the hindfoil.

The vortex convection show also great similarity to the analogous tandem cases with a pure-plunging hindfoil, as well as to the single-airfoil reference case, see Fig. 9.10.

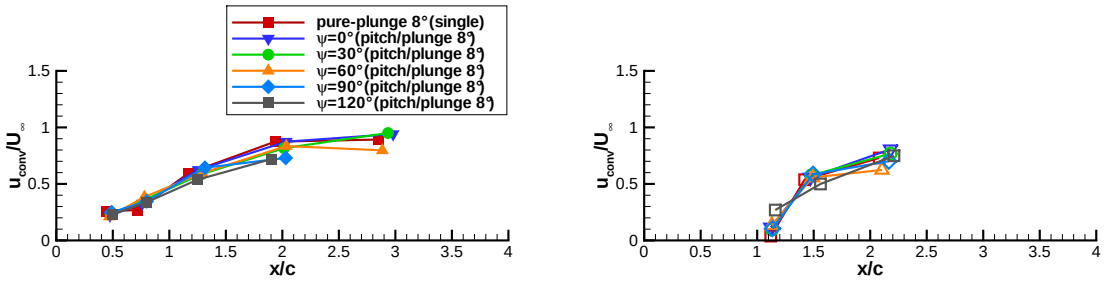

(a) LEV convection velocity

(b) TEV convection velocity

Figure 9.10: Convective velocity of LEV and TEV cores for the pitch-plunge cases.

9.3.2 Vortex-Induced Separation

Due to the pitch/plunge motion's lower effective angle of attack on the downstroke, a more attached flow is observed on its associated upstroke. Thus the vortex-induced separation in this case resembles a progression towards *deep* dynamic stall, as described in McCroskey (1982). In turn, the induced separations on the hindfoil are much stronger in nature. In fact an induced separation from the passing TEV is observed at $t/T = 0.583$ for several phase lags, i.e. $\psi = 0°$, $\psi = 30°$ and $\psi = 60°$. A comparison for various airfoil phasings is presented in Fig. 9.11. Analogous to section 8.2.3, the hindfoil for the pitch/plunge cases can be considered as strongly loaded on the associated upstroke, thus more susceptible to induced separation than for the respective unloaded pure-plunge cases.

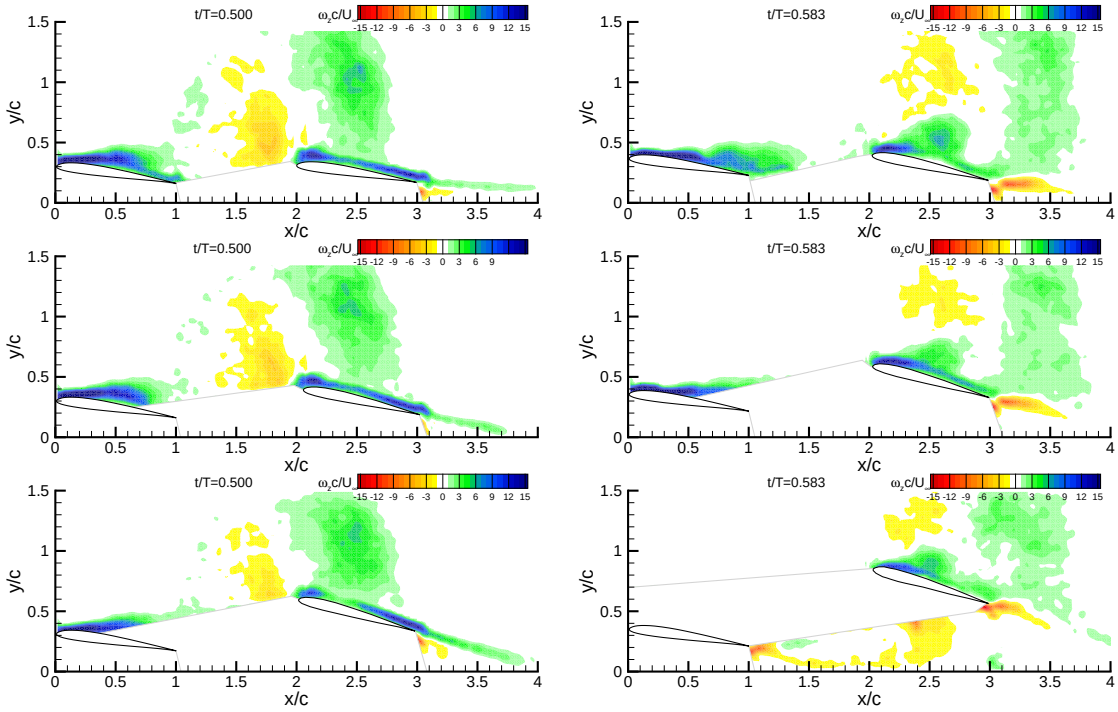

Figure 9.11: Hindfoil with pitch/plunge with $\psi = 0°$ (top), $\psi = 30°$ (middle), $\psi = 60°$ (bottom); note vortex-induced separation much stronger when compared to tandem pure-plunge cases.

9.3.3 LEV Circulation

In Fig. 9.12, as in section 9.2.3, the LEV development is substantially strengthened in the tandem-airfoil configurations. Again one can observe that the limiting formation number is significantly increased from $\hat{T} \simeq 4$ to $\hat{T} > 6$. Further to that, the LEV circulation is found to drop more drastically at higher airfoil phasings due to the interaction with the hindfoil leading edge.

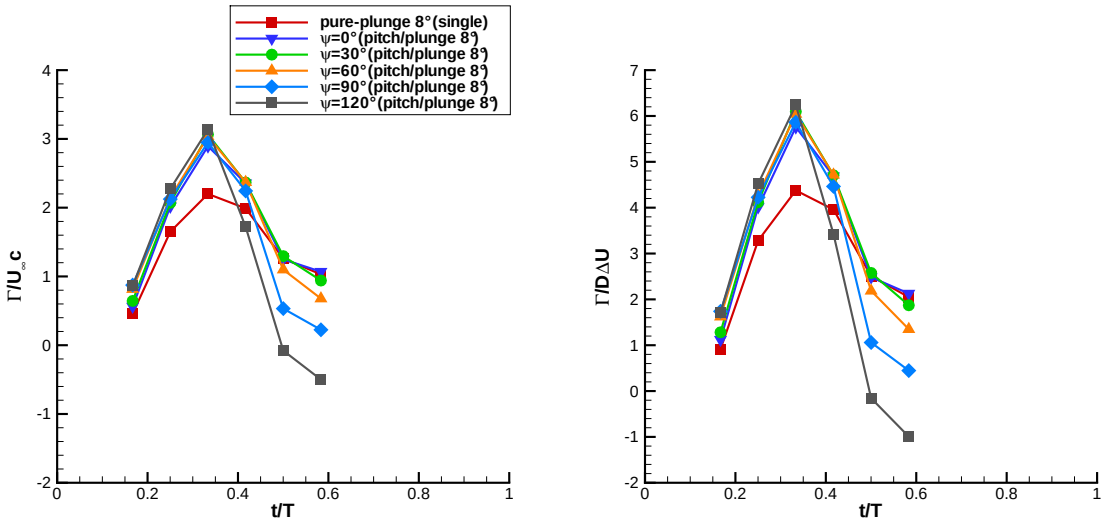

(a) circulation

(b) formation time

Figure 9.12: Development of LEV circulation (left) and formation time (right) as a function of period for the various tandem-airfoil configurations.

9.3.4 Control-Volume Analysis

For the tandem arrangement with a pitching/plunging hindfoil, the lift generation is more constant over the period, as seen in 9.13(a). Similarly in 9.13(b), the drag production is steady; albeit for higher airfoil phasings some pronounced peaks and troughs can be observed.

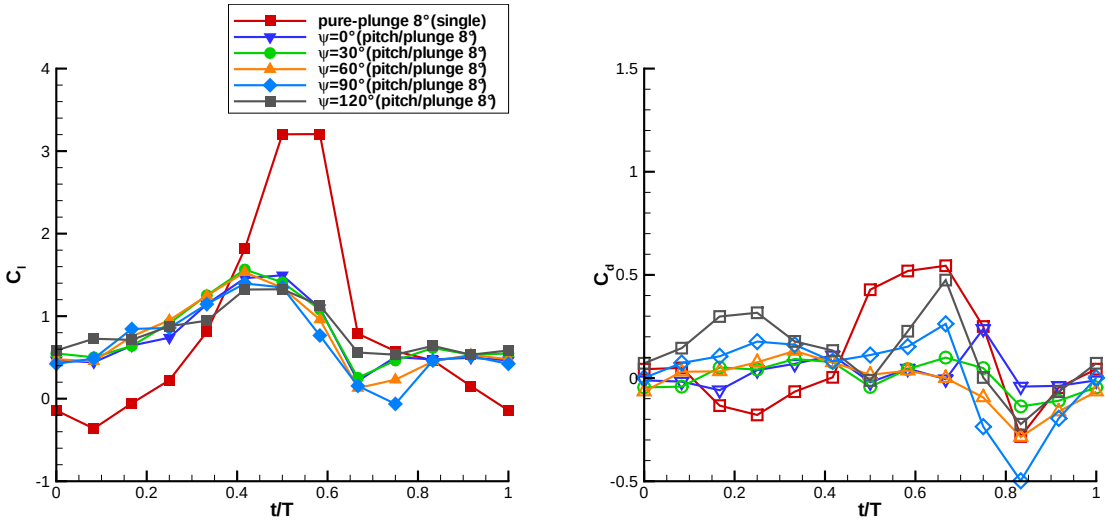

(a) lift variation

(b) drag variation

Figure 9.13: Lift and drag variation over cycle using the standard control-volume analysis; note t/T referenced to the forefoil position.

9.3.5 Pressure Integration

The pressure integration technique highlights again the advantage found for the tandem-airfoil cases. In Fig. 9.14 the induced suction due to the passing LEV-TEV pair allows for a reduction in mechanical power at the beginning of the upstroke. Despite no clear advantage in lift production, such a timing in suction can be beneficial from an energetics point of view.

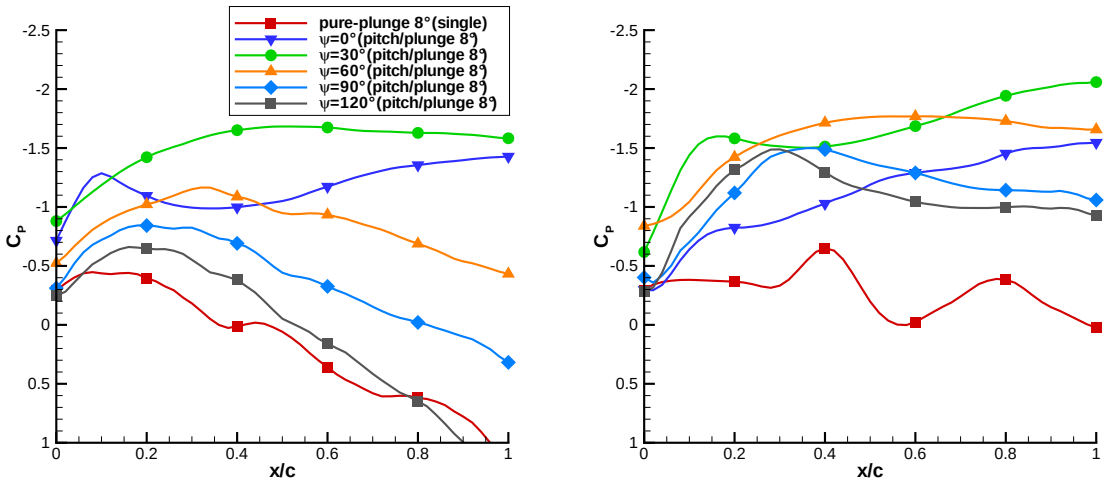

(a) $t/T = 0.500$ (b) $t/T = 0.567$

Figure 9.14: Pressure distributions over hindfoil suction surface at stroke reversal.

9.4 Insight from CFD

9.4.1 Mean Forces

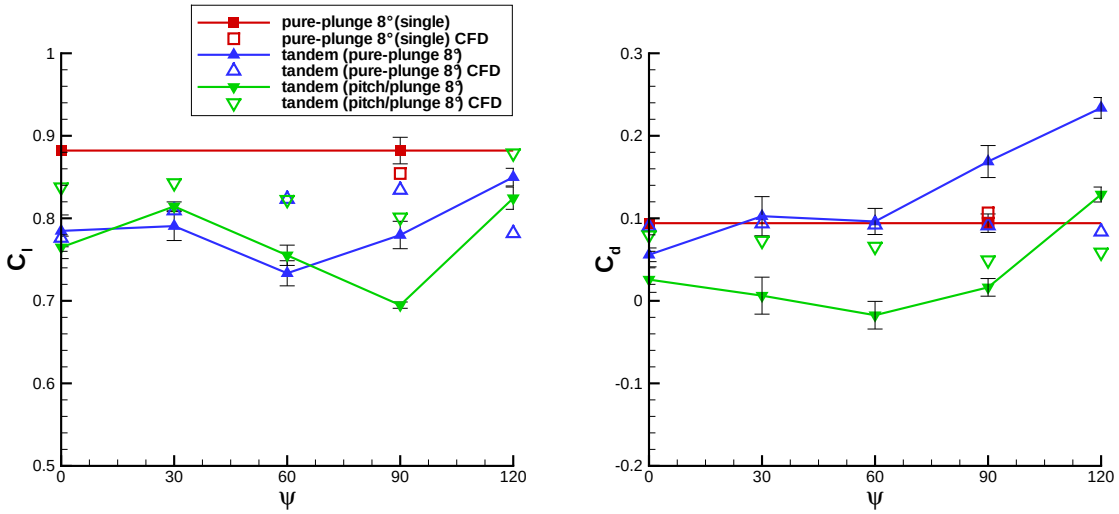

(a) mean lift (b) mean drag

Figure 9.15: Time-averaged lift and drag for both tandem arrangements from both the standard control-volume analysis (experiment) and from CFD.

When examining the mean and lift and drag forces obtained from both experiment and CFD, as in Fig 9.15, one can observe that the strong variation with airfoil phasing is underpredicted in the CFD. Based on the experimental results, no tandem configuration generates as much lift on average as the single-airfoil reference case. However, when examining drag, the $\psi = 60°$ tandem pitch/plunge case produces a slight thrust force. For all other phases, however, drag occurs and is found to grow drastically at higher airfoil phasings.

9.4.2 Time-Resolved Forces

Despite the anomalies in the force predictions from CFD, the general development, convection and interaction of the shed LEV-TEV pair agrees well with experiment. For a validation of the CFD simulations with the PIV results, see Appendix B where plots of dimensionless vorticity for both downstroke and upstroke at $\psi = 60°$ and $\psi = 90°$ are presented. In Fig. 9.16 and Fig. 9.17 the vortex interaction on the hindfoil upstroke is clearly seen at approximately time steps $t/T = 0.583$ and $t/T = 0.667$, respectively. Note that the time axis has been shifted for the hindfoil to ease the comparison with the reference cases. Of significance here is the strong leading-edge suction, which can be observed in the drag curve. This suction is particularly strong for $\psi = 90°$, whereas for $\psi = 60°$ a large overshoot in drag occurs. When comparing the forefoil curves to the single-airfoil reference cases, small discrepancies are seen due to the increase in LEV circulation, as discussed in section 9.3.3.

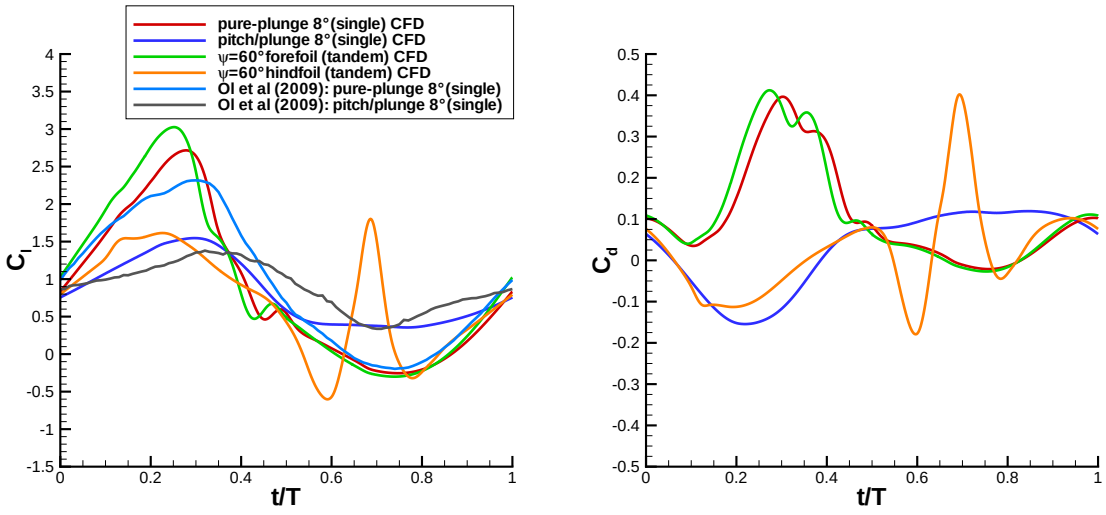

(a) lift

(b) drag

Figure 9.16: Lift and drag variation for tandem arrangement with pitch/plunge hindfoil at $\psi = 60°$; observe drop in lift and drag at approximate time step $t/T = 0.583$, note hindfoil curve shifted in time for comparison.

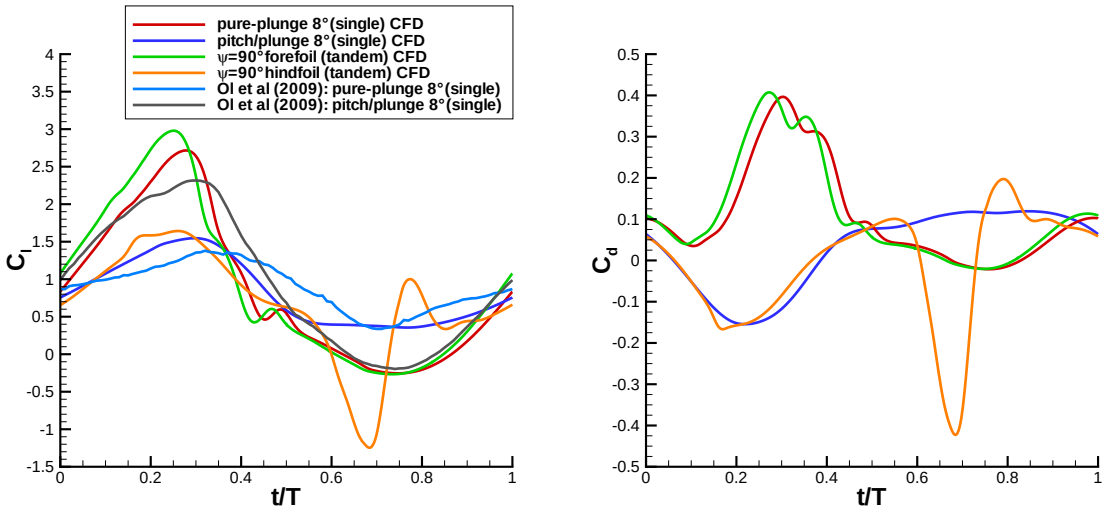

(a) lift (b) drag

Figure 9.17: Lift and drag variation for tandem arrangement with pitch/plunge hindfoil $\psi = 90°$; observe drop in lift and drag at approximate time step $t/T = 0.667$, note hindfoil curve shifted in time for comparison.

When examining the contour plots of vorticity at $t/T = 0.417$, corresponding to $t/T = 0.583$ and $t/T = 0.667$ in Figs. 9.16 and 9.17, one can clearly observe the leading-edge suction regime just below the hindfoil leading edge. The approaching LEV's downwash induces a leading-edge vortex at this position thus generating the strong thrust force. This suction bubble is particularly noticeable for the $\psi = 90°$ case. In the PIV measurements, the shadow conceals this suction region. Even without the presence of the shadow, laser reflections would limit access to this information near the airfoil surface. Therefore in this case such simple CFD simulations supplement the measurements in the wind tunnel very well.

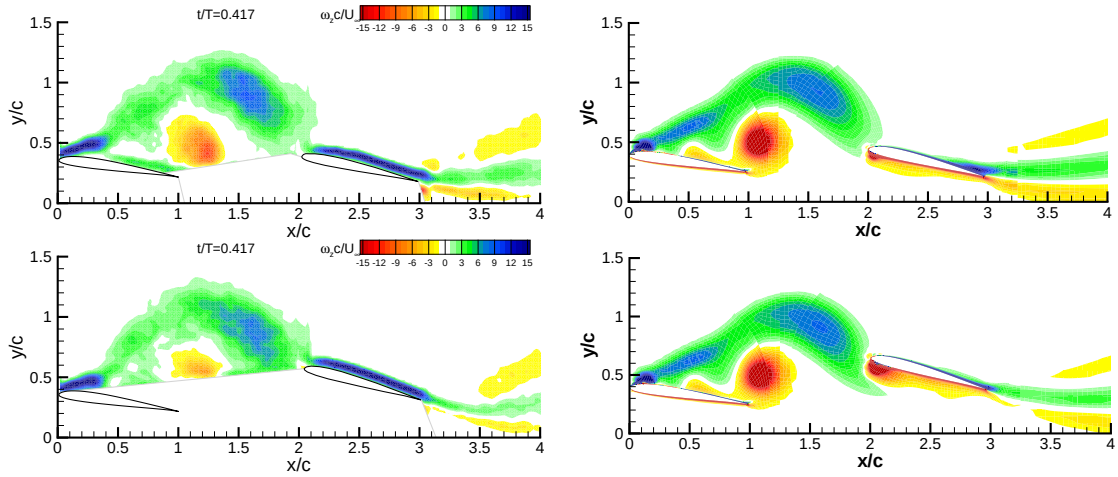

Figure 9.18: Development of leading-edge suction on forefoil for $\psi = 60°$ (top) and $\psi = 90°$ (bottom): experiment (left) and CFD (right), where time is referenced to forefoil motion. Note leading-edge suction in experiment not visible due to shadow.

9.4.3 Power Consumption

When considering power consumption, as discussed in section 2.4.2, the timing of the normal force relative to the airfoil plunge velocity becomes critical. In Fig. 9.19 it is apparent that a slight increase in power consumption can be observed for the forefoil when compared to the reference case. However, on the hindfoil, the passing of the LEV over the hindfoil is responsible for vortex-induced separation (see section 9.3.2), which in turn generates a strong suction in the normal direction.

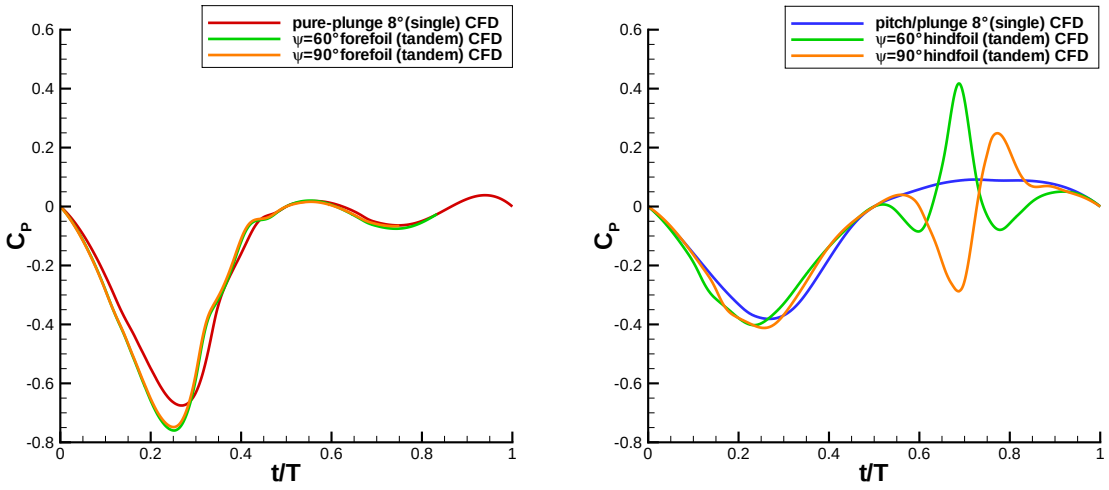

(a) forefoil (b) hindfoil

Figure 9.19: Variation in power for tandem arrangements with pitch/plunge hindfoil ($\psi = 60°$ and $\psi = 90°$) where energy extraction is observed on upstroke; note hindfoil curve shifted in time for comparison.

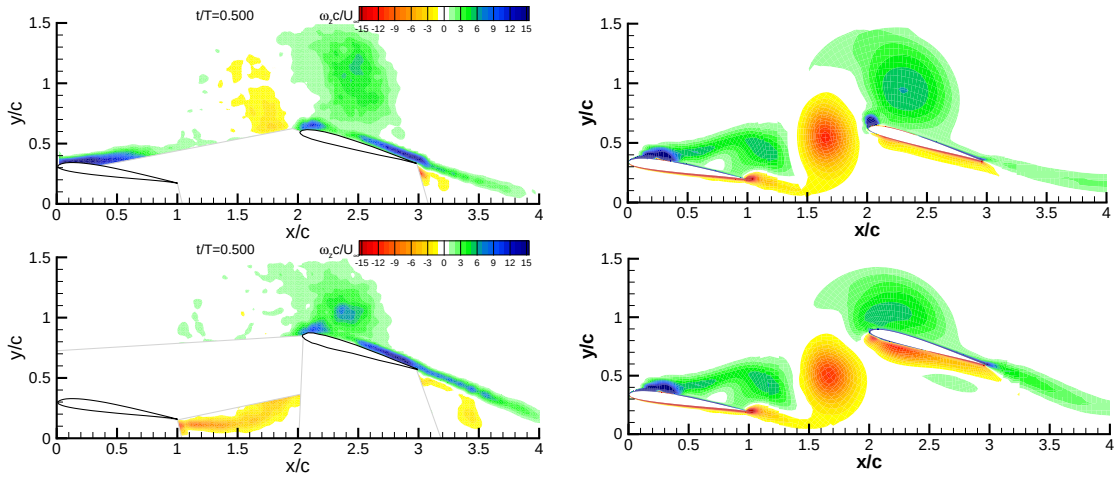

Figure 9.20: Development of normal suction on forefoil for $\psi = 60°$ (top) and $\psi = 90°$ (bottom) responsible for power reduction: experiment (left) and CFD (right), where time is referenced to forefoil motion.

Again referring to plots of dimensionless vorticity at the corresponding time step of $t/T = 0.5$ ($t/T = 0.667$ and $t/T = 0.75$ in Fig. 9.19), the suction responsible for reducing power consumption is clearly observed, both in experiment and CFD. The approaching TEV induces an upwash at the leading edge - in contrast to the downwash effect of the LEV in section 9.4.2 - such that a strong and compact separation bubble is

generated over the suction surface. From these results one can surmise that the timing of such an interaction, when considering power reduction, is very sensitive to the position and plunging velocity of the hindfoil, such that the $\psi = 60°$ case shows a substantial improvement over the $\psi = 90°$ case simply due to the hindfoil velocity at the time of interaction and not due to the strength of the induced suction itself.

9.5 Summary

The vortex interaction of two moving airfoils in tandem configuration has been examined experimentally using PIV in the wind tunnel and with simple URANS simulations. For both pure-plunge and pitch/plunge hindfoil configurations, strong vortex-induced separation was observed at low airfoil phasings when the TEV passed over the hindfoil. For medium airfoil phasings ($30° \leq \psi \leq 60°$), the TEV collided with the hindfoil's leading edge, at times initiating separation. For high airfoil phasings ($\psi \geq 90°$), the shed vortex pair was split such that the LEV and TEV traveled overtop and beneath the hindfoil, respectively. A control-volume analysis of the various cases concluded that no tandem case could produce, on average, as much lift as the single-airfoil reference case. A net thrust, however, was identified for the tandem arrangement with a pitching and plunging hindfoil at $\psi = 60°$. With the help of CFD, the cause for net thrust was identified by the generation of a strong leading-edge suction bubble caused by the induced downwash of the forefoil LEV. For the same airfoil phasing but at a later time step, the upwash induced by the shed TEV caused a vortex-induced separation on the hindfoil upstroke, which was responsible for reducing power consumption. This suction induced by the passing TEV was also observed experimentally through the pressure integration of the PIV velocity field overtop of the airfoil.